Supplement of Weather Clim. Dynam., 7, 1853–1874, 2026
https://doi.org/10.5194/wcd-7-1853-2026-supplement

Supplement of

Dynamics of the Asian Summer Monsoon Anticyclone: insights from potential vorticity tendency diagnostics

Ninghui Li et al.

Correspondence to: Jonathon S. Wright (jswright@tsinghua.edu.cn) and Jie Gao (jgaots2017@163.com)

Table of Contents

Table S1. Statistics of vortices in each month of boreal summer from 2000-2020

	Time	Overall	Persistent Vortex		Transient Vortex	
		Count	Count	Percentage	Count	Percentage
ERA5 (2000-2020)	Total	24940	16370	65.64%	8570	34.36%
	May	4012	2179	54.31%	1833	45.29%
	June	4510	2805	62.20%	1705	37.80%
	July	5272	3703	70.24%	1569	29.76%
	August	5655	4096	72.43%	1559	27.57%
	September	5491	3587	65.33%	1904	34.67%
JRA-3Q (2000-2020)	Total	24702	16099	65.17%	8603	34.83%
	May	3931	2023	51.46%	1908	48.54%
	June	4466	2801	62.72%	1665	37.28%
	July	5231	3716	71.04%	1515	28.96%
	August	5607	3975	70.89%	1632	29.11%
	September	5467	3584	65.56%	1883	34.44%
Merra2 (2000-2020) ASM	Total	25579	14448	56.48%	11131	43.52%
	May	4067	2023	49.74%	2044	50.26%
	June	4774	2463	51.59%	2311	48.41%
	July	5234	2998	52.28%	2236	42.72%
	August	5906	3707	62.77%	2199	37.23%
	September	5598	3257	58.18%	2341	41.82%
CIESM/BASE (2000-2018)	Total	23551	15797	67.08%	7754	32.92%
	May	3882	2362	60.84%	1520	39.16%
	June	3921	2783	70.98%	1138	29.02%
	July	5390	3552	65.90%	1838	34.10%
	August	5409	3649	67.46%	1762	32.54%
	September	4949	3451	69.73%	1798	30.27%

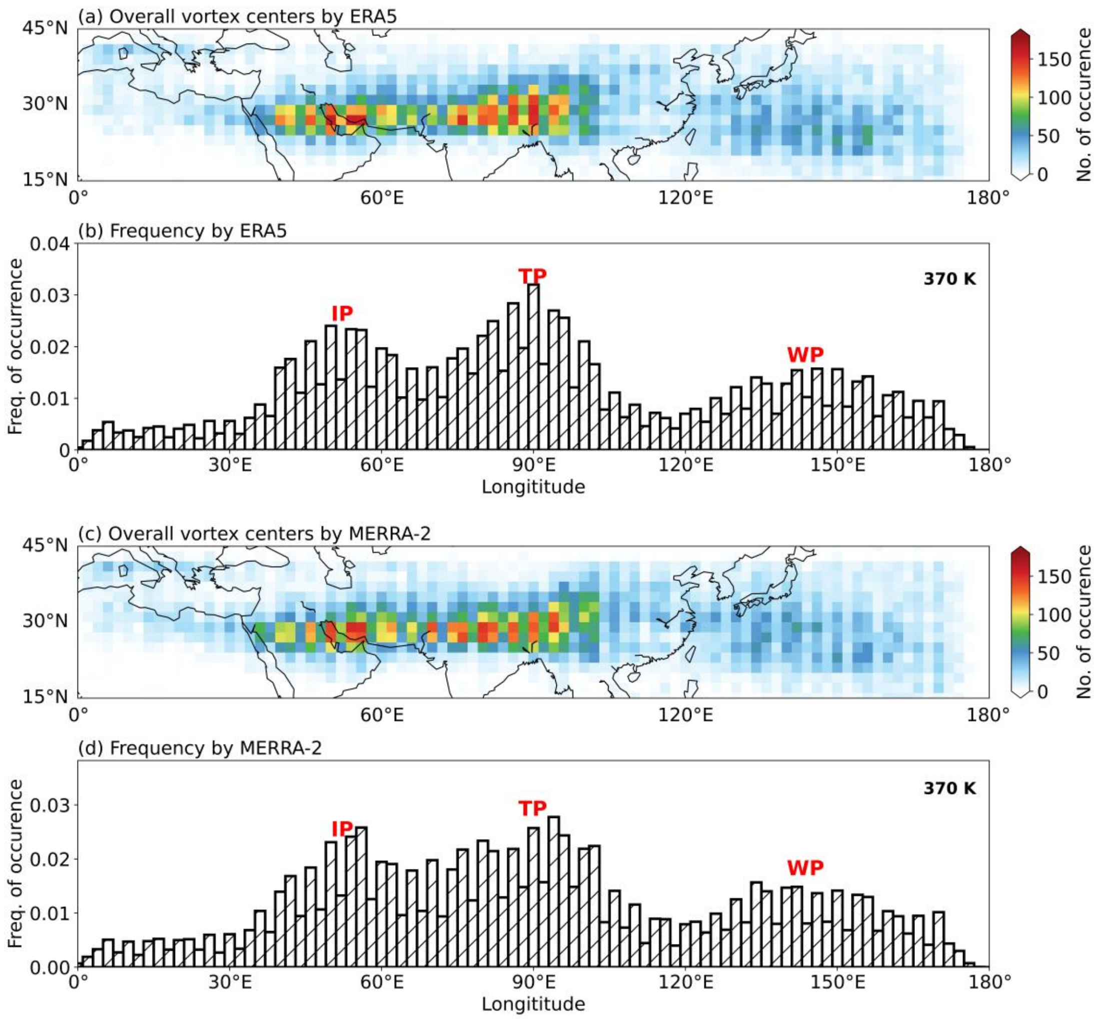

Figure S1. The spatial distributions of occurrence frequency of the anticyclone centers at isentropic 370 K using (a, b) ERA5, (c, d) MERRA-2, during May–September 2000–2020. The "IP" refers to the Iranian Plateau mode, "TP" refers to the Tibetan Plateau mode, and "WP" refers to the Western Pacific mode.

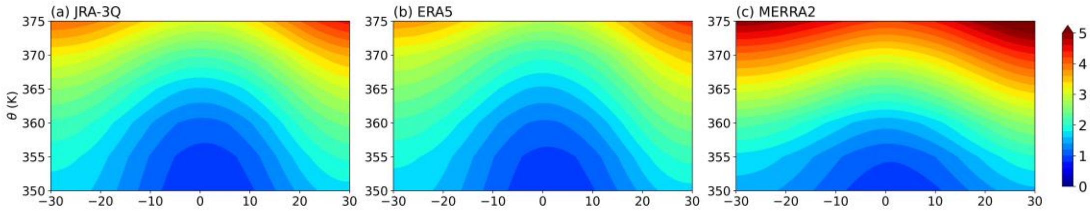

Figure S2. Vertical-longitude distribution of potential vorticity (unit: PVU, where 1 PVU = 10^{-6} m^2 K s^{-1} kg^{-1}) from 350-375 K for (a) JRA-3Q, (b) ERA5, and (c) MERRA2. The PV field is a composite mean around the vortex center generated by the vortex tracking algorithm described in the main text.

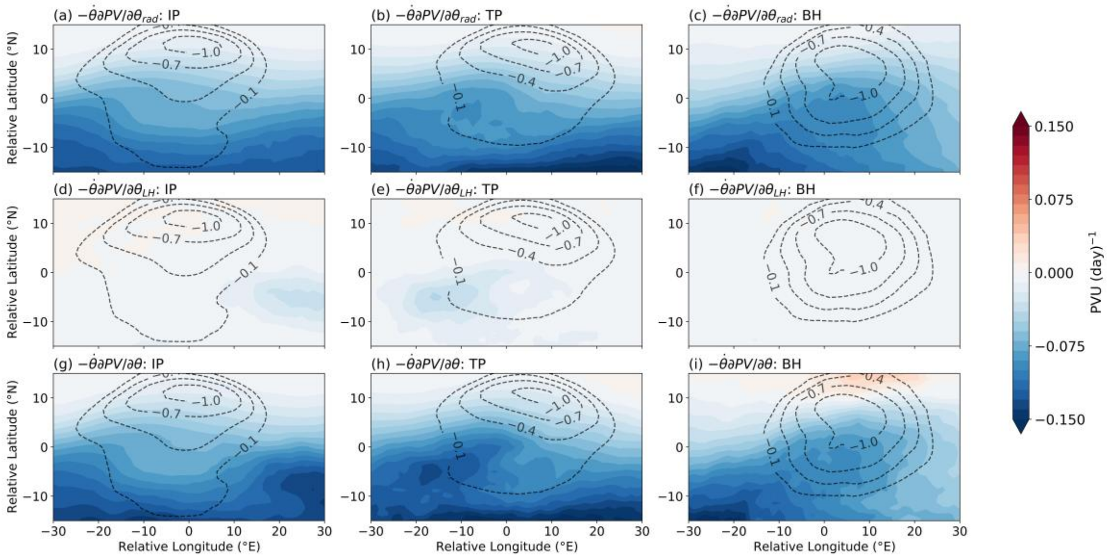

Figure S3. The PV tendency from diabatic vertical advection due to (a)-(c) radiative heating, (d)-(f) latent heating, and (g)-(i) total diabatic heating for vortices associated with each of the three modes on the 370 K level based on JRA-3Q. Black dashed contours show the PV anomaly at 370 K, with contours from –1 to –0.1 PVU at an interval of 0.3 PVU. Results are shown for the (a,d,g) Iranian Plateau (IP), (b,e,h) Tibetan Plateau (TP), and (c,f,i) Bonin High vortex modes.

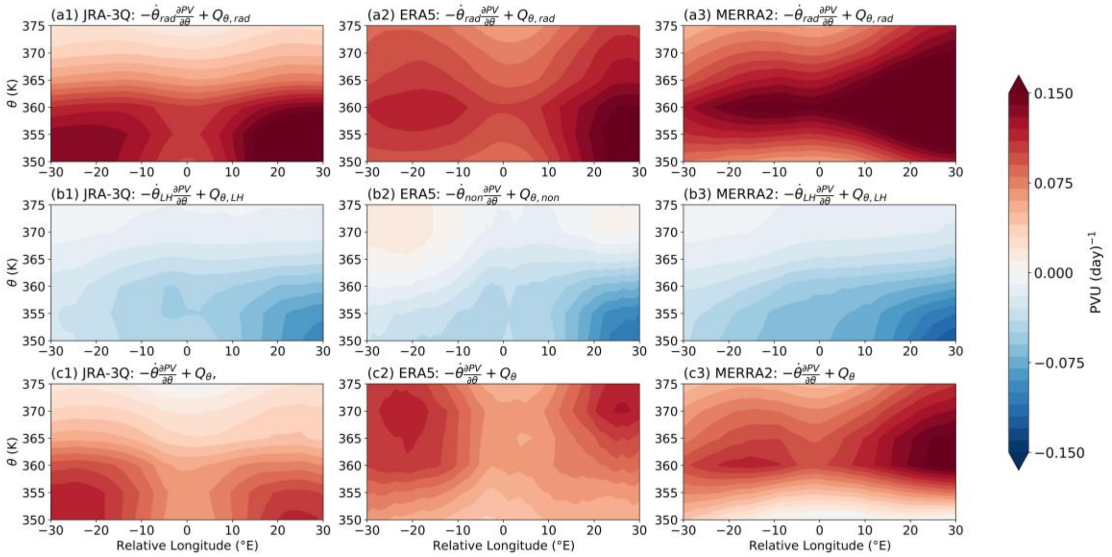

Figure S4. The sum of vertical divergence and diabatic heating terms for (a1)-(a3) radiative heating, (b1)-(b3) latent heating or non-radiative heating, and (c1)-(c3) total diabatic heating. From left to right, the columns are ERA5, JRA-3Q and MERRA2.

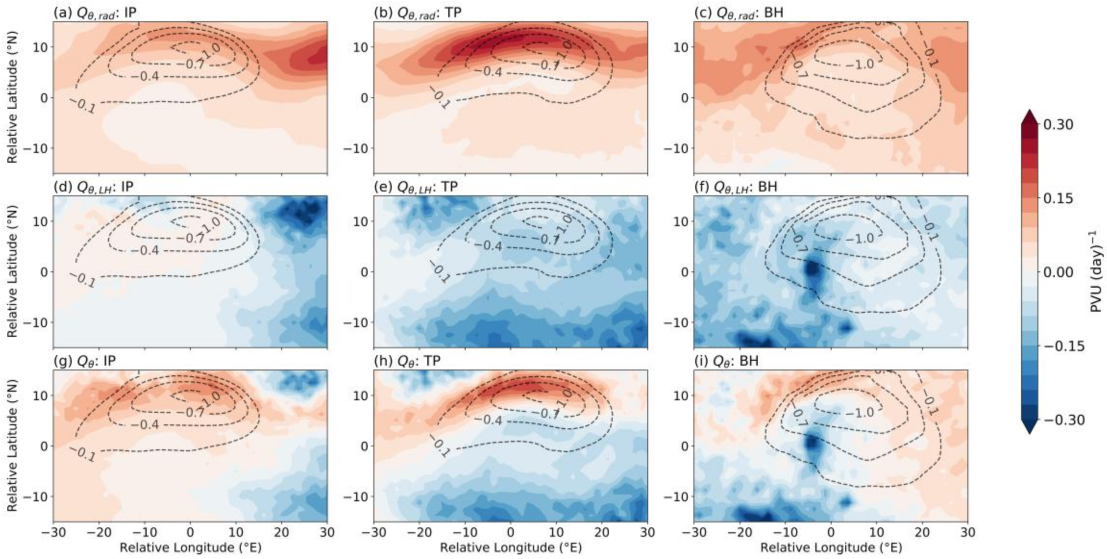

Figure S5. PV tendencies from the vertical divergence of (a)-(c) radiative heating, (d)-(f) latent or non-radiative heating, and (g)-(i) their sum on the 350 K isentropic surface based on ERA5. Results are shown for the (a,d,g) Iranian Plateau (IP), (b,e,h) Tibetan Plateau (TP), and (c,f,i) Bonin High vortex modes. Black dashed contours show the PV anomaly at 350 K from −1 to –0.1 PVU at an interval of 0.3 PVU. The horizontal and vertical axes indicate longitude and latitude relative to the vortex center, respectively.

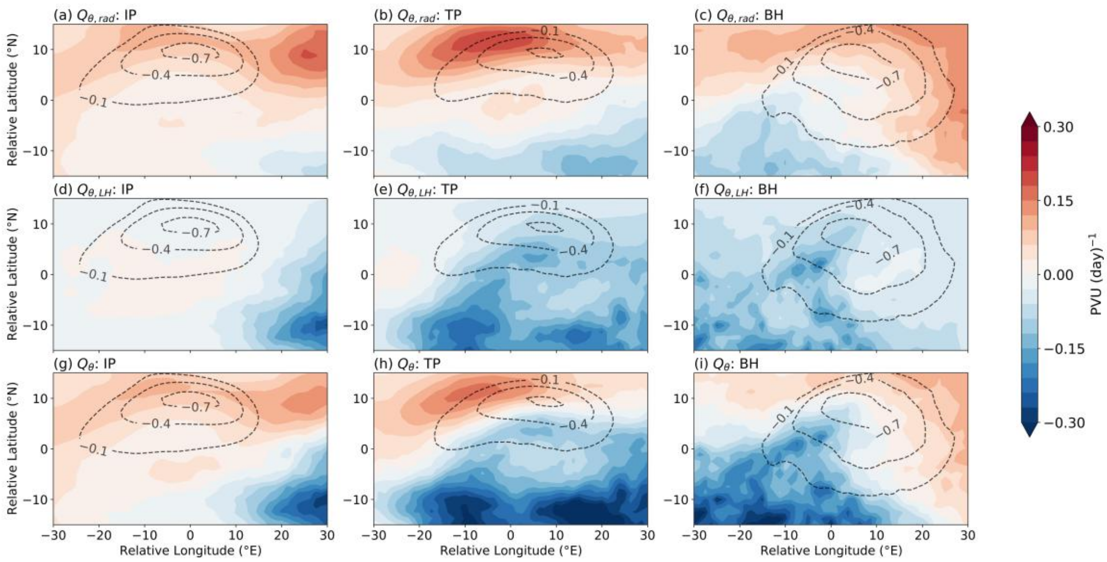

Figure S6. The same as Fig. S5, but for MERRA2**.**

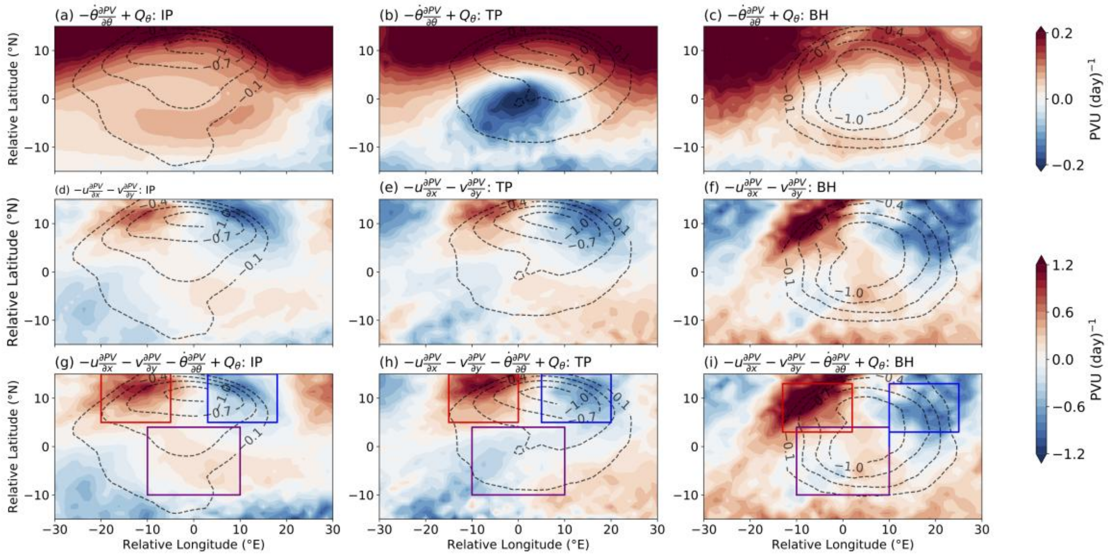

Figure S7. PV tendencies from ERA5 due to (a)-(c) the vertical divergence of diabatic heating and diabatic vertical advection, (d)-(f) horizontal advection, and (g)-(i) their sum on the 370 K isentropic surface for vortices in the Iranian Plateau (IP; left), Tibetan Plateau (TP; center), and Bonin High (BH; right) modes. Black dashed contours show PV anomalies at 370 K ranging from −1 to –0.1 PVU at an interval of 0.3 PVU. The horizontal and vertical axes indicate longitude and latitude relative to the vortex center, respectively. The red boxes in the lower row indicate the main areas of net positive PV tendencies, while the blue boxes indicate regions of net negative PV tendencies.

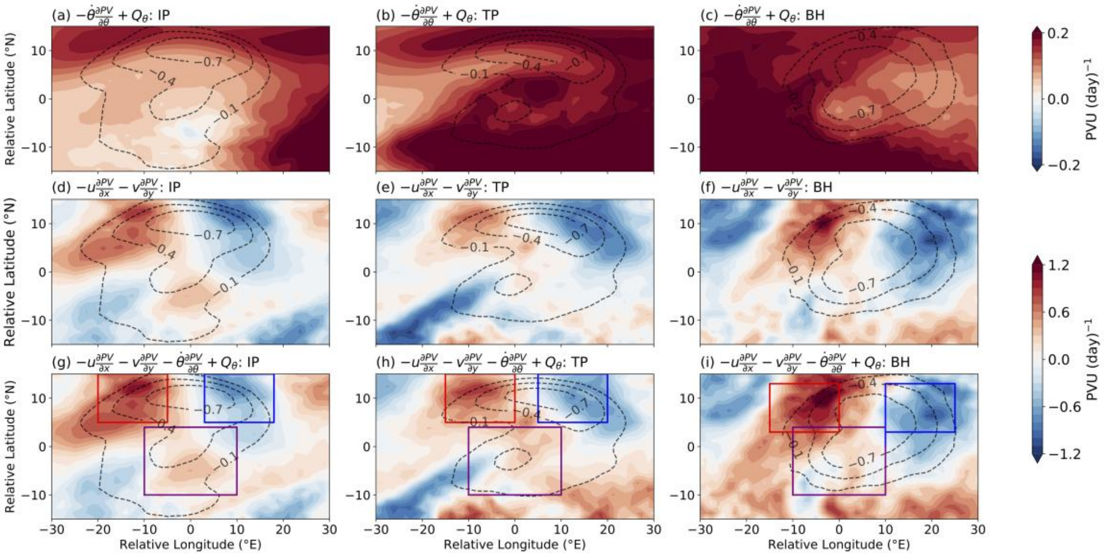

Figure S8. The same as Fig. S7, but for MERRA2**.**

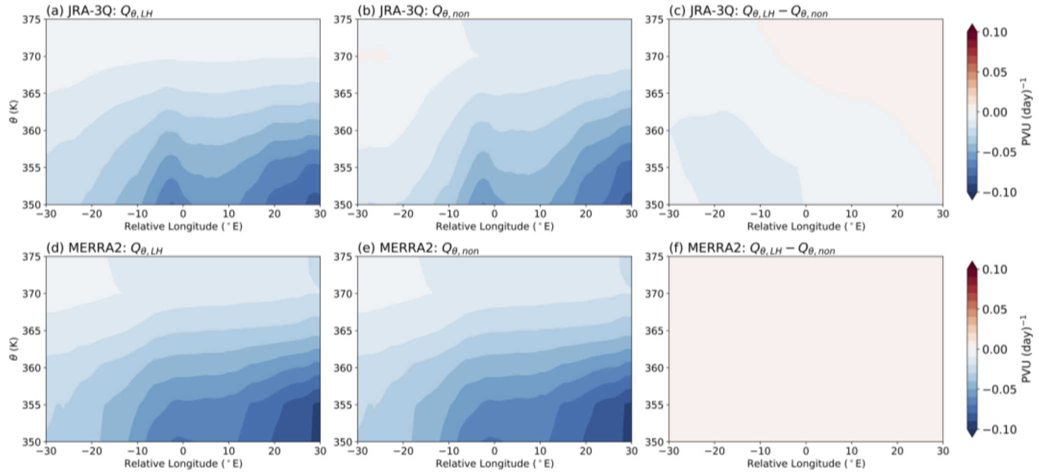

Figure S9. Vortex-relative distributions of Q_θ in longitude and potential temperature based on (a)-(c) JRA-3Q and (d)-(f) MERRA-2: (a,d) moist-physics heating; (b,e) non-radiative heating; and (c,f) the difference between the two. All vortices are included in the composite, as in Fig. 9b of the main text. For JRA-3Q, moist-physics heating is defined as cnvhr + lrghr (the sum of temperature tendencies due to convection and due to large-scale condensation) and non-radiative heating is defined as cnvhr + lrghr + vdfhr, where vdfhr is the temperature tendency due to parameterized turbulent mixing. For MERRA-2, moist-physics heating is defined as DTDTMST (temperature tendency due to moist physics and non-radiative heating as DTDTTOT – DTDTRAD (the difference of the temperature tendency due to all model physics and the temperature tendency due to radiative heating).

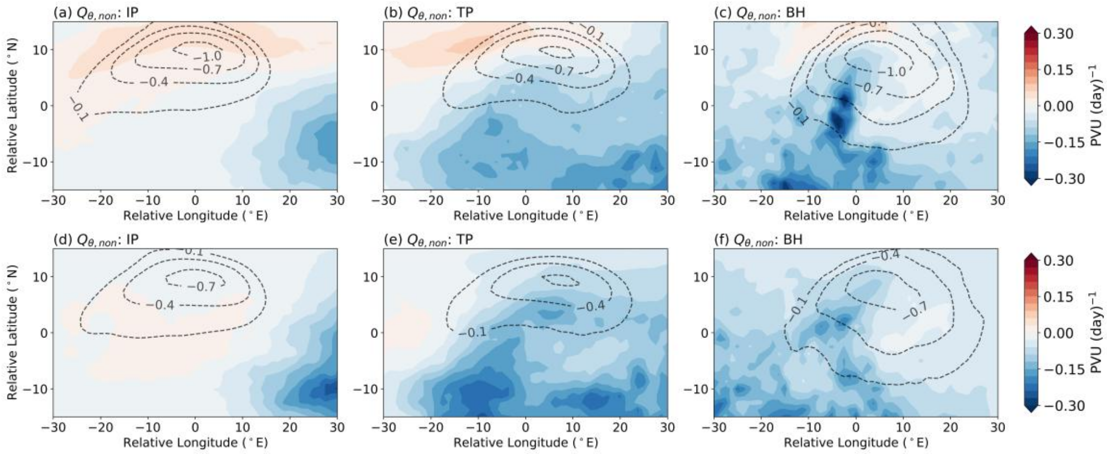

Figure S10. Vortex-relative distributions of diabatic heating-related terms based on (a)-(c) JRA-3Q and (d)-(f) MERRA-2 using heating from all radiative processes rather than only moist physics (cf. Fig. 10d-f; Fig. S6d-f). Columns correspond to vortices belonging to the Iranian Plateau (IP), Tibetan Plateau (TP), and Western Pacific/Bonin High (BH) vortex modes. The overall consistency between the non-radiative and moist-physics approaches estimates illustrates the weak sensitivity of the diagnosed diabatic PV tendencies to the choice of convective heating representation, supports the use of non-radiative heating as a proxy for moist-physics heating in ERA5, and establishes the robustness of the main conclusions to this choice.